

Statistical Majorana Bound State Spectroscopy

Alexander Ziesen,¹ Alexander Altland,² Reinhold Egger,³ and Fabian Hassler¹

¹*JARA Institute for Quantum Information, RWTH Aachen University, 52056 Aachen, Germany*

²*Institut für Theoretische Physik, Universität zu Köln, Zülpicher Straße 77, 50937 Köln, Germany*

³*Institut für Theoretische Physik, Heinrich-Heine-Universität, D-40225 Düsseldorf, Germany*

(Dated: December 26, 2022)

Tunnel spectroscopy data for the detection of Majorana bound states (MBS) is often criticized for its proneness to misinterpretation of genuine MBS with low-lying Andreev bound states. Here, we suggest a protocol removing this ambiguity by extending single shot measurements to sequences performed at varying system parameters. We demonstrate how such sampling, which we argue requires only moderate effort for current experimental platforms, resolves the statistics of Andreev side lobes, thus providing compelling evidence for the presence or absence of a Majorana center peak.

Introduction.—About a decade after the first proposals for MBS engineering in topological quantum devices [1–5], numerous reports of experimental signatures have been published, see, e.g., Refs. [6–11]. However, opinions remain divided as to whether “Majoranas have been seen” or not. Broadly speaking, experiments aimed at MBS detection can be categorized into two groups: tunnel spectroscopy detecting midgap resonances caused by the assumed presence of an MBS [12–16], and experiments going after unambiguous intrinsic properties of topological states, from unconventional noise correlations [17–25] to full-feathered braiding protocols [26–29]. While the second group remains at the level of theoretical proposals, the former are straightforwardly realizable as a part of the core MBS experiments. However, the downside is that tunnel spectroscopy data can be prone to misinterpretation. Among various other candidates for midgap signatures, pairs of conventional Andreev bound states — which in symmetry class D [30] superconductor environments¹ have a tendency to cluster around zero energy — may leave experimental signatures hard to distinguish from a single MBS [31–39]. At any rate, as witnessed by the current debate on the “topological gap protocol” by the Microsoft Quantum team [11, 40, 41], the community at large does not appear to be ready to take tunnel spectroscopy signatures, even of high quality, as unambiguous evidence for MBS formation.

In this paper, we propose a relatively effortless upgrade from single shot tunnel spectroscopy measurements to parametric sequences of measurements. Their realization for individual samples neither requires essential new hardware nor measurement protocols beyond what is already available. We argue that the compounded measurement data collected by statistical tunnel spectroscopy *does* contain compelling evidence for or against MBS formation. Crucially, both the presence and the

absence of an MBS will leave unique imprints, provided the required statistical resolution has been met. A second key feature is that disorder or device imperfections, usually considered as unwelcome obstructions to MBS observability [42–46], here assume the role of a resource: our approach works best for significantly disordered systems.

To understand its principle, we need to recall a few signatures of the spectrum of class D superconductors [30, 31]. In confined geometries subject to disorder or other sources of “integrability breaking”, the Andreev spectrum is discrete, symmetric around zero energy, and subject to statistical level correlations. Specifically, in the absence of topological midgap states, Andreev bound states exhibit a slight statistical tendency to attraction to zero energy, while they repel amongst themselves. Conversely, if a topological midgap state is present, Andreev states get pushed away from zero energy, and still repel amongst themselves. These signatures find a quantitative representation in the ensemble-averaged spectral density [31],

$$\langle \rho(\epsilon) \rangle = \frac{1+c}{2} \delta(\epsilon) + \frac{1}{\delta_\epsilon} \left(1 - c \frac{\sin(2\pi\epsilon/\delta_\epsilon)}{2\pi\epsilon/\delta_\epsilon} \right), \quad (1)$$

where δ_ϵ is the average (Andreev bound state) energy-spacing and $c = +1$ ($c = -1$) in the presence (absence) of a MBS. The sinusoidal oscillations in Eq. (1) describe a tendency of the spectrum to “crystallize” into a statistically uniform sequence around zero, with diminishing ($\sim \epsilon^{-1}$) rigor. Equation (1) encodes a nonlocal fragmentation of the Hilbert space and is obtained under the idealizing assumption of an infinite ensemble subject to disorder strong enough to couple a large number of levels (random matrix limit [47]).

In experimental reality, there is no mathematical ensemble, disorder may not be quite so strong, and the recorded tunnel conductance data contains wave function fluctuations next to spectral signatures. Further, the MBS peak, if present, will be broadened by spectroscopic resolutions, temperature, and possibly other forms of environmental coupling. However, as we are going to

¹ Strictly speaking, the system is either in class B or in class D depending on whether a MBS is present or not. For simplicity, we refer to both cases as “class D”.

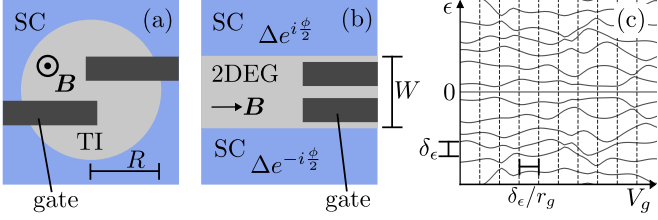


FIG. 1. Schematic of statistical spectroscopy setups. (a) A vortex defined by a TI coated with an s -wave superconductor (SC, blue region) except for a region of radius R which is threaded by ν magnetic flux quanta. Electrostatic finger gates serve to effectively change the disorder configuration. (b) Alternative setup: a planar Josephson junction with electrostatic gates and in-plane magnetic field. (c) Typical in-gap spectrum vs gate voltage V_g for the setup in (a). By varying V_g , Andreev state energy levels change on a scale set by the level spacing δ_ϵ . Sequences of independent disorder realizations are separated by $\delta V_g \approx \delta_\epsilon/r_g$ (see main text) as marked by the vertical lines.

argue, and demonstrate by numerical simulations, even relatively small *sequences of measurements* performed for an engineered ensemble of configurations at limited resolution can reveal the principal signature of the spectral data: a statistical oscillation of period δ_ϵ with opposite sign, depending on the presence or absence of Majorana states. In other words, a positive sign signal assumes the role of a control measurement revealing sufficient resolution for what in the presence of a MBS must flip sign to become a negative sign sequence. These rigidity patterns are deeply non-perturbative signatures of the class D spectrum, which in the $c = 1$ case do require a *single* midgap state (*aka* Majorana). On this basis, we reason that a “smoking gun” signature is at hand. While our approach applies to arbitrary Majorana platforms, we illustrate it below for the example of a proximitized topological insulator (TI) slab pierced by a vortex [48–54], where Andreev states correspond to Caroli-de Gennes-Matricone subgap states [55].

Statistical spectroscopy principles.—We propose a protocol where an effectively averaged spectral density $\langle \rho(\epsilon) \rangle$ is obtained from a single disorder realization via an average over one (or several) control parameters. This parameter space may be realized, e.g., by variation of magnetic field strengths, or of gate electrode voltages applied to quantum wires or planar Josephson junctions, as indicated in Fig. 1(b). As a concrete example, we here formulate the approach for a TI vortex, cf. Fig. 1(a): An s -wave superconductor is deposited on a TI surface except for a circular region of radius R . Through this region an integer number, ν , of superconducting flux quanta $\Phi_0 = \pi/e$ is threaded ($\hbar = 1$ throughout). For odd parity of ν , this synthetic vortex binds a zero energy MBS [49].

Variations in the voltage of nearby finger gates, V_g , parametrically change the effective system Hamiltonian. They will realize an effective ensemble average, provided

the perturbation is strong enough to effectively scramble the spectrum of vortex states, cf. Fig. 1(c). To estimate the required voltage variations, we make the conservative assumption that the Coulomb interaction across the vortex is strongly screened, and that only local wave functions right under the geometric finger gate surface are susceptible to the perturbation. To first order in perturbation theory, this leads to the estimate $\langle \Psi | \delta V_g | \Psi \rangle \approx \delta V_g \int_g d^2r |\Psi_r|^2 \approx r_g \delta V_g$ for the distortion of the energy, ϵ , of individual states. Here, the integral extends over the area underneath the gate, we assume approximate statistical uniformity of the wave function modulus, and $0 \leq r_g \leq 1$ is the fraction of the gate area relative to that of the vortex. Variations $\delta V_g \gtrsim \delta_\epsilon/r_g$ strong enough that the perturbation exceeds the level spacing, δ_ϵ , effectively define a new realization of the spectrum, cf. Fig. 1(c).

Provided the broadening, κ , of Andreev states due to disorder exceeds the level spacing δ_ϵ , we expect level repulsion, and in the consequence the emergence of the spectral density in Eq. (1) upon averaging over an ensemble. Presently, this ensemble average is realized by sampling a large number of configurations distinguished by changes $\delta V_g r_g / \delta_\epsilon = \mathcal{O}(1)$, and subsequently collecting the results in a histogram.

In a concrete experiment where each level spacing is divided into N_b bins and the number of runs is N_r , an average number of $n_b = N_r/N_b$ levels will be counted per bin. This number is subject to statistical fluctuations $\delta n_b \sim \mathcal{O}(n_b^{1/2})$. To obtain a reliable result, the relative fluctuation $\delta n_b/n_b$ must be smaller than the relative change $|\rho(\epsilon) - \rho(\infty)|/\rho(\infty)$, computed according to Eq. (1). A straightforward estimate for, say, $\epsilon \approx 2\delta_\epsilon$ leads to the conclusion that $N_r \sim 10^2 N_b$ runs are required to obtain statistical certainty.

TI vortex.—In the following, we test the statistical protocol for the TI vortex setup in Fig. 1(a). The single-particle Bogoliubov-de Gennes Hamiltonian describing the proximitized TI surface is given by [49]

$$H_{\text{BdG}} = (v\mathbf{p} \cdot \boldsymbol{\sigma} - \mu)\tau_z + \text{Re } \Delta(\mathbf{r}) \tau_x - \text{Im } \Delta(\mathbf{r}) \tau_y, \quad (2)$$

where v is the surface-state velocity, μ the chemical potential, and Pauli matrices τ_i (σ_i) act in particle-hole (spin) space. In the London gauge, the pair potential is $\Delta(\mathbf{r}) = |\Delta(r)|e^{-iv\theta}$, with polar coordinates (r, θ) relative to the vortex center and $\Delta(r) = \Delta \Theta(r - R)$ assumed as step function like. The Hamiltonian (2) satisfies particle-hole symmetry, $\mathcal{C}H_{\text{BdG}}\mathcal{C}^{-1} = -H_{\text{BdG}}$ with $\mathcal{C} = \sigma_y \tau_y K$ and K complex conjugation, placing it into symmetry class D. (For completeness, we mention that in the field free case, $\nu = 0$, we also have time reversal symmetry, $\mathcal{T}H_{\text{BdG}}\mathcal{T}^{-1} = H_{\text{BdG}}$ with $\mathcal{T} = i\sigma_y K$, implying an upgrade to class DIII.)

We add disorder to the vortex core $r < R$ in the form of a Gaussian correlated random potential $V(\mathbf{r})\tau_z$ with zero mean and variance $\langle V(\mathbf{r})V(\mathbf{r}') \rangle = \gamma^2 \delta(\mathbf{r} - \mathbf{r}')$. The corresponding scattering mean free path computed in Born

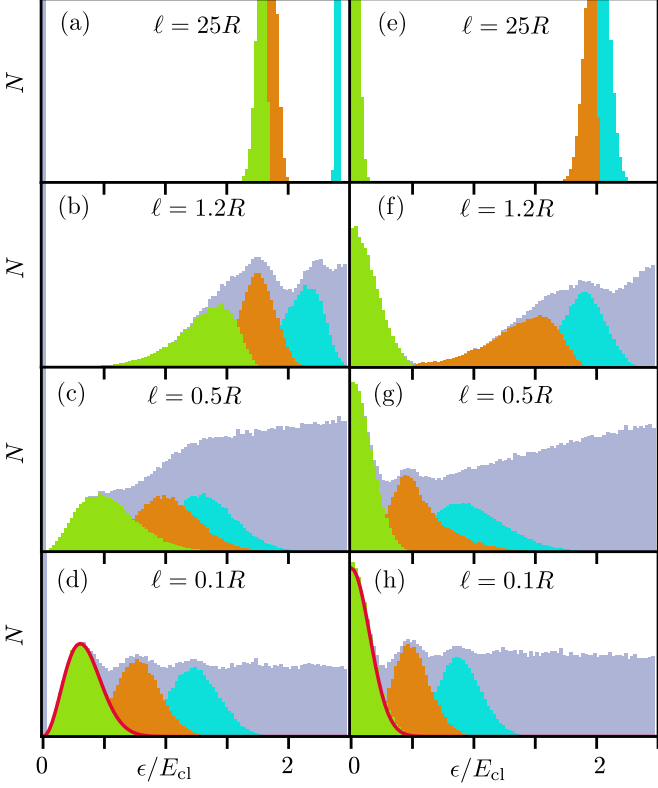


FIG. 2. Histogram for the positive energy levels of the TI vortex, with energies in units of $E_{\text{cl}} = v/R$. Panels (a)–(d) [(e)–(h)] show numerical results in the presence [absence] of a MBS with increasing disorder strength as obtained by diagonalizing H_{BDG} for $N_r = 5 \times 10^4$ disorder realizations. Green, orange and cyan colors refer to the three lowest levels, all others are represented by the grey background. For weak disorder, $\ell \gg R$ [panels (a,e)], the averaged spectral peaks lie isolated, they begin to overlap when $\ell \sim R$ [panels (b,c) and (f,g)], and finally combine to a continuum described by Eq. (1) at $\ell < R$ [panels (d,h)]. The statistics of the lowest level is accurately described by the spacing distribution $P(\epsilon)$ (red curves) discussed in the text.

approximation is given by $\ell = v/\kappa = (v/\gamma)^2 R$. Comparison with the bound-state spacing of the clean vortex, $\delta_\epsilon \simeq v/R \equiv E_{\text{cl}}$, shows that the threshold to strong disorder mixing, $\delta_\epsilon \sim \kappa$, is reached when $\ell \sim R$, i.e., when the quasi-particle motion crosses over from ballistic to diffusive. For stronger disorder, the characteristic level spacing shrinks to $\delta_\epsilon \simeq (\ell/R)(v/R) \equiv E_{\text{Th}}$, i.e., from the inverse of the ballistic time of flight, E_{cl} , to the inverse of the diffusion time across the vortex, E_{Th} , see the SM [56] for details.

Our statistical approach to MBS spectroscopy works for disorder beyond the ballistic/diffusive threshold. To illustrate this point, Fig. 2 shows data histograms obtained from $N_r = 5 \times 10^4$ disorder realizations and for disorder strengths ranging from an almost perfectly ballistic regime, $\ell = 25R$, to a diffusive one with $\ell = 0.1R$. The columns on the left (right) are for a vortex with (with-

out) MBS, realized here by setting $\nu = 1$ ($\nu = 2$). In the ballistic regime, we observe weakly broadened states with spacings varying strongly at scales $\sim E_{\text{cl}}$. Upon crossing into the diffusive regime, they start to overlap, along with a tendency towards a more uniform spacing — the level crystallization symptomatic for quantum chaotic spectra.

Real experiments have access to the cumulative contribution of all levels, here indicated in grey, where we observe the gradual approach to the profile in Eq. (1), as well as to the distribution of individual levels, cf. the green/orange/cyan histograms for the lowest three positive energy levels. For disorder deep in the diffusive regime, we expect the statistics of these levels to be described by the principles of random matrix theory [47]. Specifically, for class D one expects the probability distribution for the lowest lying level in the case with [without] MBS to be given by $P(\epsilon) \propto \epsilon^2 \exp(-\epsilon/2)$ [$P(\epsilon) \propto \exp(-\epsilon^2/2)$] [30, 56]. Figure 2 shows that these distributions, indicated as red curves, are clearly realized by the disordered vortex in the strong disorder regime. However, the most important conclusion is that the presence or absence of a MBS is clearly resolved via the statistics of the cumulative histogram, provided the focus of attention is shifted to the side bands, and the disorder is sufficient to induce inter-level correlations.

Experimental reality.—The analysis above assumed arbitrary energy resolution, and averaging over a large number $\mathcal{O}(10^5)$ of realizations. What happens under less ideal conditions? In an experiment, the potential $V(\mathbf{r})$ describing impurities or scattering off device irregularities is fixed and different realizations of the spectrum are generated by variation of externally adjustable parameters. In the TI vortex, the magnetic field strength is likewise fixed, which leaves gate electrodes as the next best choice for generating a parameter set. To generate $N_r \sim 10^2 N_b$ samples required for N_b bins per level spacing (see above estimate), one may need to work with f finger gates and the resulting f -dimensional parameter space. As the gate voltages are meant to mimic “disorder”, it is best to use an asymmetric geometric design as indicated in Fig. 1. Electrodes with large electrode-to-vortex area ratio, r_g , will generate optimal sensitivity of energy levels, $\sim r_g V_g$.

The simulations discussed in the following were performed for $N_b = 10$ bins, requiring $N_r = \mathcal{O}(10^3)$ runs. We worked with $f = 3$ electrodes [56], and varying each of their voltages over a range $\delta V_g \sim \delta_\epsilon/r_g$ generated the parameter space for up to $N_r \approx 10^4$ statistically independent samples ². Finally, we account for the broadening of individual levels due to temperature or environmental coupling by introducing a Lorentzian line width,

² If no independent information on the characteristic level spacing δ_ϵ is available, the latter may be estimated by measuring the spacing between peaks in the averaged spectral density.

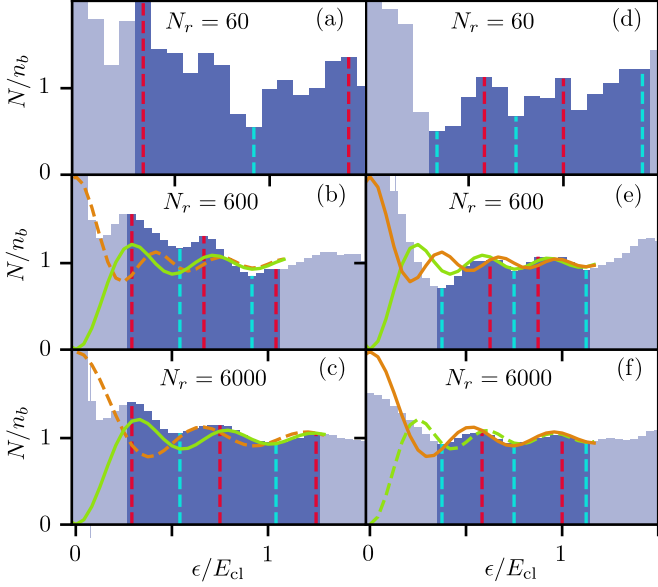


FIG. 3. Histogram as in Fig. 2 but for a single realization of $V(\mathbf{r})$ with $\ell = 0.1R$, using an increasing number of N_r samples with (left column) and without (right) MBS. The first five extrema are indicated by dashed vertical lines. The green (orange) curves are fits to Eq. (1) for $c = 1$ ($c = -1$) within the dark blue regions, i.e., with the δ -peak removed, using δ_ϵ as single fit parameter. Inferior fits are shown as dashed curves.

$\delta(\epsilon) \mapsto (\Gamma/\pi)/(\epsilon^2 + \Gamma^2)$, with $\Gamma = 0.05E_{\text{cl}}$. Here, $\Gamma \lesssim \delta_\epsilon$ is required to resolve the oscillatory pattern of the target spectral density, i.e., our method requires the resolvability of individual states ³.

Given this setup, the minimal goal is a statistically sound distinction between the cases $c = \pm 1$ in Eq. (1). Figure 3 illustrates how the two cases are distinguished through a phase shift in the oscillatory spectral density *at finite energy*. In either case, a midgap peak is present (caused by a broadened MBS for $c = +1$, or a statistical accumulation of Andreev states for $c = -1$). While these two peaks are difficult to distinguish, our method focuses on the spectrum away from the center. We note that in either case, the average spectral density contains a sequence of extrema at $\epsilon \sim \frac{2n+1}{4}\delta_\epsilon$. The difference is that this sequence starts with a maximum (for $c = 1$) or a minimum (for $c = -1$). A more refined signature is obtained by subtracting a constant background and fitting the remaining oscillatory signal for the first, say, five extrema to Eq. (1), using δ_ϵ as single fit parameter.

Fig. 3 shows data processed in this way for increasing number of runs N_r , either with (left column) and without (right) MBS. The quality of the data may be assessed, e.g., by calculating the sum of squared distances between the extrema of the fit function and the data. For too low sample number, e.g., for $N_r = 60$, no unambiguous pattern of extrema is identifiable. At $N_r = 600$ samples, side lobes begin to emerge, but a reliable assignment of extrema is still difficult to ascertain. However, for $N_r = 6000$, the extremal energies are evenly spaced, and the squared distance fit accurately determines the correct sign of c . Additional information on system parameters, such as knowledge of the effective broadening Γ , may be exploited to develop more informed fitting protocols for the ensemble averaged data. However, we found that such refinements lead only to minor improvements of the results.

Let us briefly comment on the experimental feasibility of the TI vortex setup. Generally speaking the vortex area should be chosen small enough that its quantized levels can be resolved, and large enough that neighboring levels are coupled by disorder and gate variations. With $\delta_\epsilon \approx E_{\text{Th}} = v\ell/R^2$, and given typical values $v \approx 5 \times 10^5 \text{ m/s}$, $\ell \approx 20 \text{ nm}$ [57], with spectral resolution $\Gamma \approx 30 \mu\text{eV}$, one needs to have $R \lesssim 3 \mu\text{m}$. Choosing $R = 300 \text{ nm}$ and finger gates of width $\approx 50 \text{ nm}$, we have $\ell/R \approx 0.1$. For these values, individual levels can be distinguished and a few finger gate electrodes could be placed over the vortex core. We are thus confident that the requirements for our proposal to work are met by existing setups.

Conclusions.—We have proposed a novel scheme for the detection of MBS in existing device structures which combines tunnel spectroscopy with elements of statistics. The focus of attention is here shifted from the center peak ubiquitous in spectroscopic data — which is notorious for its misinterpretability — to the pattern of side bands. The unavoidable presence of effective disorder becomes a resource in that it induces correlations between levels which, upon averaging over different parametric realizations, lead to the effectively crystalline structure in Eq. (1). The latter originates in a combination of statistics and topology which is unambiguously linked to the presence or absence of a MBS, even if the latter cannot be clearly identified in isolation. Another advantage of the approach is that it includes its own validation: If neither the positive, $c = 1$, nor the negative, $c = -1$, signal can be resolved, the method has not been implemented with sufficient accuracy. The principal conditions for it to work are resolvability of individual levels (where one may argue that this condition must be met anyway for the MBS to become a useful resource), sufficient statistics provided by at least $\mathcal{O}(10^3)$ runs, and effective disorder strong enough to cause level correlation. (If the “native” disorder is too weak, one may contemplate lowering the level spacing by increasing the vortex size for diagno-

³ Another source of uncertainty is due to the fact that tunnel spectroscopy measures point conductance, i.e., a quantity proportional to the product of spectral density and wave function moduli, where the latter remain unknown. However, one may expect that in a large data set, these variations efficiently average out.

tic purposes.) These criteria are realistic for the vortex platform, and we are confident that the same holds for other realizations, such as planar Josephson junctions, leaving sufficient freedom for the placement of gate electrodes. We conclude that this approach has the potential to settle the issue of MBS existence with available measurement protocols and hardware.

We thank Y. Ando and J. Schluck for discussions. We acknowledge funding by the Deutsche Forschungsgemeinschaft (DFG, German Research Foundation), Projekt-nummer 277101999 – TRR 183 (AA and RE, projects A01, A03, B04, and C01), and under Germany’s Excellence Strategy – Cluster of Excellence Matter and Light for Quantum Computing (ML4Q) EXC 2004/1 – 390534769.

[1] J. Alicea, *Rep. Prog. Phys.* **75**, 076501 (2012).

[2] M. Leijnse and K. Flensberg, *Semiconductor Science and Technology* **27**, 124003 (2012).

[3] C. W. J. Beenakker, *Annual Review of Condensed Matter Physics* **4**, 113 (2013).

[4] S. DasSarma, M. Freedman, and C. Nayak, *njp Quantum Inf.* **1**, 51001 (2015).

[5] P. Marra, *Journal of Applied Physics* **132**, 231101 (2022).

[6] V. Mourik, K. Zuo, S. M. Frolov, S. R. Plissard, E. P. A. M. Bakkers, and L. P. Kouwenhoven, *Science* **336**, 1003 (2012).

[7] S. Nadj-Perge, I. K. Drozdov, J. Li, H. Chen, S. Jeon, J. Seo, A. H. MacDonald, B. A. Bernevig, and A. Yazdani, *Science* **346**, 602 (2014).

[8] R. M. Lutchyn, E. P. A. M. Bakkers, L. P. Kouwenhoven, P. Krogstrup, C. M. Marcus, and Y. Oreg, *Nat. Rev. Mat.* **3**, 52 (2018).

[9] Q. Liu, C. Chen, T. Zhang, R. Peng, Y.-J. Yan, C.-H.-P. Wen, X. Lou, Y.-L. Huang, J.-P. Tian, X.-L. Dong, G.-W. Wang, W.-C. Bao, Q.-H. Wang, Z.-P. Yin, Z.-X. Zhao, and D.-L. Feng, *Phys. Rev. X* **8**, 041056 (2018).

[10] M. Li, G. Li, L. Cao, X. Zhou, X. Wang, C. Jin, C.-K. Chiu, S. J. Pennycook, Z. Wang, and H.-J. Gao, *Nature* **606**, 890 (2022).

[11] MicrosoftQuantum, “Inas-al hybrid devices passing the topological gap protocol,” (2022), arXiv:2207.02472.

[12] K. Sengupta, I. Žutić, H.-J. Kwon, V. M. Yakovenko, and S. Das Sarma, *Phys. Rev. B* **63**, 144531 (2001).

[13] K. T. Law, P. A. Lee, and T. K. Ng, *Phys. Rev. Lett.* **103**, 237001 (2009).

[14] K. Flensberg, *Phys. Rev. B* **82**, 180516 (2010).

[15] H.-H. Sun, K.-W. Zhang, L.-H. Hu, C. Li, G.-Y. Wang, H.-Y. Ma, Z.-A. Xu, C.-L. Gao, D.-D. Guan, Y.-Y. Li, C. Liu, D. Qian, Y. Zhou, L. Fu, S.-C. Li, F.-C. Zhang, and J.-F. Jia, *Phys. Rev. Lett.* **116**, 257003 (2016).

[16] A. Zazunov, R. Egger, and A. Levy Yeyati, *Phys. Rev. B* **94**, 014502 (2016).

[17] C. J. Bolech and E. Demler, *Phys. Rev. Lett.* **98**, 237002 (2007).

[18] J. Nilsson, A. R. Akhmerov, and C. W. J. Beenakker, *Phys. Rev. Lett.* **101**, 120403 (2008).

[19] A. Golub and B. Horovitz, *Phys. Rev. B* **83**, 153415 (2011).

[20] A. Haim, E. Berg, F. von Oppen, and Y. Oreg, *Phys. Rev. Lett.* **114**, 166406 (2015).

[21] D. E. Liu, M. Cheng, and R. M. Lutchyn, *Phys. Rev. B* **91**, 081405 (2015).

[22] K. M. Tripathi, S. Das, and S. Rao, *Phys. Rev. Lett.* **116**, 166401 (2016).

[23] T. Jonckheere, J. Rech, A. Zazunov, R. Egger, and T. Martin, *Phys. Rev. B* **95**, 054514 (2017).

[24] T. Jonckheere, J. Rech, A. Zazunov, R. Egger, A. L. Yeyati, and T. Martin, *Phys. Rev. Lett.* **122**, 097003 (2019).

[25] J. Manousakis, C. Wille, A. Altland, R. Egger, K. Flensberg, and F. Hassler, *Phys. Rev. Lett.* **124**, 096801 (2020).

[26] D. Aasen, M. Hell, R. V. Mishmash, A. Higginbotham, J. Danon, M. Leijnse, T. S. Jespersen, J. A. Folk, C. M. Marcus, K. Flensberg, and J. Alicea, *Phys. Rev. X* **6**, 031016 (2016).

[27] C. W. J. Beenakker, *SciPost Phys. Lect. Notes* **15** (2020).

[28] K. Flensberg, F. von Oppen, and A. Stern, *Nat. Rev. Mat.* **6**, 944 (2021).

[29] B. Sbierski, M. Geier, A.-P. Li, M. Brahlk, R. G. Moore, and J. E. Moore, *Phys. Rev. B* **106**, 035413 (2022).

[30] A. Altland and M. R. Zirnbauer, *Phys. Rev. B* **55**, 1142 (1997).

[31] D. Bagrets and A. Altland, *Phys. Rev. Lett.* **109**, 227005 (2012).

[32] J. Liu, A. C. Potter, K. T. Law, and P. A. Lee, *Phys. Rev. Lett.* **109**, 267002 (2012).

[33] R. Aguado, *Riv. Nuovo Cimento* **40**, 523 (2017).

[34] C. Moore, T. D. Stanescu, and S. Tewari, *Phys. Rev. B* **97**, 165302 (2018).

[35] A. Vuik, B. Nijholt, A. R. Akhmerov, and M. Wimmer, *SciPost Phys.* **7**, 061 (2019).

[36] E. Prada, P. San-Jose, M. W. A. de Moor, A. Geresdi, E. J. H. Lee, J. Klinovaja, D. Loss, J. Nygård, R. Aguado, and L. P. Kouwenhoven, *Nat. Rev. Phys.* **2**, 225 (2020).

[37] M. Valentini, F. Peñaranda, A. Hofmann, M. Brauns, R. Hauschild, P. Krogstrup, P. San-Jose, E. Prada, R. Aguado, and G. Katsaros, *Science* **373**, 82 (2021).

[38] P. Yu, J. Chen, M. Gomenko, G. Badawy, E. P. A. M. Bakkers, K. Zuo, V. Mourik, and S. Frolov, *Nat. Phys.* **17**, 482 (2021).

[39] L. C. Contamin, L. Jarjat, W. Legrand, A. Cottet, T. Kontos, and M. R. Delbecq, *Nature Communications* **13**, 6188 (2022).

[40] S. Frolov and V. Mourik, (2022), majorana fireside podcast, <https://youtu.be/RnYghkDaHH0>.

[41] A. R. Akhmerov, (2022), what can we learn from the reported discovery of Majorana states? Journal Club Condensed Matter, see https://doi.org/10.36471/JCCM_July_2022_01.

[42] A. R. Akhmerov, J. P. Dahlhaus, F. Hassler, M. Wimmer, and C. W. J. Beenakker, *Phys. Rev. Lett.* **106**, 057001 (2011).

[43] M. Wimmer, A. R. Akhmerov, J. P. Dahlhaus, and C. W. J. Beenakker, *New Journal of Physics* **13**, 053016 (2011).

[44] P. W. Brouwer, M. Duckheim, A. Romito, and F. von Oppen, *Phys. Rev. Lett.* **107**, 196804 (2011).

[45] M. Diez, I. C. Fulga, D. I. Pikulin, J. Tworzydło, and C. W. J. Beenakker, *New Journal of Physics* **16**, 063049

(2014).

[46] A. Haim and A. Stern, *Phys. Rev. Lett.* **122**, 126801 (2019).

[47] M. L. Mehta, *Random Matrices* (Academic Press, 2004).

[48] L. Fu and C. L. Kane, *Phys. Rev. Lett.* **100**, 096407 (2008).

[49] M. Z. Hasan and C. L. Kane, *Rev. Mod. Phys.* **82**, 3045 (2010).

[50] P. A. Ioselevich, P. M. Ostrovsky, and M. V. Feigel'man, *Phys. Rev. B* **86**, 035441 (2012).

[51] R. S. Akzyanov, A. V. Rozhkov, A. L. Rakhmanov, and F. Nori, *Phys. Rev. B* **89**, 085409 (2014).

[52] H. S. Røising, R. Ilan, T. Meng, S. H. Simon, and F. Flicker, *SciPost Phys.* **6**, 055 (2019).

[53] A. Ziesen and F. Hassler, *Journal of Physics: Condensed Matter* **33**, 294001 (2021).

[54] B. S. de Mendonça, A. L. R. Manesco, N. Sandler, and L. G. G. V. D. da Silva, “Can caroli-de gennes-matricon and majorana vortex states be distinguished in the presence of impurities?” (2022), arXiv:2204.05078.

[55] C. Caroli, P. De Gennes, and J. Matricon, *Physics Letters* **9**, 307 (1964).

[56] See the online Supplementary Material (SM), where we provide additional details on peak spacing distributions, on the mean free path, and on our numerical simulations.

[57] A. A. Taskin, Z. Ren, S. Sasaki, K. Segawa, and Y. Ando, *Phys. Rev. Lett.* **107**, 016801 (2011).

Supplementary Material to “Statistical Majorana Bound State Spectroscopy”

Alexander Ziesen,¹ Alexander Altland,² Reinhold Egger,³ and Fabian Hassler¹

¹*JARA Institute for Quantum Information, RWTH Aachen University, 52056 Aachen, Germany*

²*Institut für Theoretische Physik, Universität zu Köln, Zülpicher Straße 77, 50937 Köln, Germany*

³*Institut für Theoretische Physik, Heinrich-Heine-Universität, D-40225 Düsseldorf, Germany*

We here derive the distribution function $P(\epsilon)$ from random matrix theory (see Sec. I), discuss the mean free path ℓ (see Sec. II), and provide details on our numerical calculations in Sec. III. Equation or figure numbers containing the index 'M' refer to the main text.

I. DISTRIBUTION FUNCTIONS

Analytical results for the distribution function $P(\epsilon)$ of the lowest finite-energy level ϵ can be obtained by random matrix theory arguments [1]. In practice, it is sufficient to calculate $P(\epsilon)$ for the smallest nontrivial matrix dimension d for the corresponding class D random matrix ensemble, where $d = 3$ ($d = 2$) with (without) a MBS. Using independent real-valued normal-distributed random variables, $\{a, b, c\}$, the respective random matrices are written as

$$V_{d=3} = \begin{pmatrix} 0 & -a & -b \\ a & 0 & -c \\ b & c & 0 \end{pmatrix}, \quad V_{d=2} = \begin{pmatrix} 0 & -a \\ a & 0 \end{pmatrix}. \quad (1)$$

The particle-hole symmetric spectrum is then given by $\{0, \pm\lambda_3 = \pm\sqrt{a^2 + b^2 + c^2}\}$ for $d = 3$, and by $\{\pm\lambda_2 = \pm|a|\}$ for $d = 2$. Expressing the dependence on $\{a, b, c\}$ in terms of multivariate χ^2 -distributions, we obtain the distributions

$$P(\lambda_3) = \sqrt{\frac{2}{\pi}}\lambda_3^2 e^{-\lambda_3^2/2}, \quad P(\lambda_2) = \sqrt{\frac{2}{\pi}}e^{-\lambda_2^2/2}. \quad (2)$$

The energy distribution, $P(\epsilon)$, with $\epsilon = \lambda_3$ or $\epsilon = \lambda_2$, respectively, now follows as quoted in the main text.

II. MEAN FREE PATH

The mean free path ℓ connects the disorder strength γ to experimentally accessible quantities for the TI vortex platform. Using the Born approximation and the density of states $D_2(\epsilon) = |\epsilon|/(2\pi v^2)$ obtained from Eq. (M2), the energy-dependent mean free path is given by

$$\ell = \frac{v}{2\pi\gamma^2 D_2(\epsilon)} = \frac{v^3}{\gamma^2 |\epsilon|}. \quad (3)$$

For low-energy in-gap states, Eq. (3) is evaluated at $\epsilon = \delta_\epsilon$, with δ_ϵ the level spacing. Depending on the hierarchy of ℓ and R , δ_ϵ is either given by the ballistic ($\delta_\epsilon \simeq E_{\text{cl}} = v/R$) or by the diffusive ($\delta_\epsilon \simeq E_{\text{Th}} = v\ell/R^2$) Thouless scale. In the respective limits, we then obtain

$$\ell \approx \begin{cases} \frac{v^2}{\gamma^2} R, & \gamma \ll v, \\ \frac{v}{\gamma} R, & \gamma \gg v. \end{cases} \quad (4)$$

Thus, δ_ϵ and ℓ both are suppressed by a factor of v/γ in the diffusive regime.

III. NUMERICAL SIMULATION DETAILS

We present details about the numerical simulations employed to verify the gate-based sampling method. The full Bogoliubov-de Gennes (BdG) Hamiltonian in the presence of the Gaussian random potential $V(\mathbf{r})$ is $H = H_{\text{BdG}} + V(\mathbf{r})\tau_z$ with H_{BdG} in Eq. (M2). For an etched vortex, the radial profile of the pairing gap is well approximated by $|\Delta(\mathbf{r})| = \Delta \Theta(r - R)$. Moreover, for low-energy in-gap states, we can effectively capture the effects of the superconductor as a boundary condition at $r = R$ which follows by sending $\Delta \rightarrow \infty$. Below we use the quantum numbers $\alpha = (n, m)$, with the (integer or half-integer) angular momentum m and the (integer) radial quantum number n . Introducing also the dimensionless radial variable $x_\alpha = \epsilon_\alpha r/v$ for finite energy $\epsilon_\alpha \neq 0$, the corresponding eigenstates of H_{BdG} for $\mu = \Delta = 0$ are expressed in terms of Bessel functions,

$$f_\alpha(\mathbf{r}) = \mathcal{N}_\alpha e^{im\theta} \begin{pmatrix} ie^{-i(\nu+1)\theta/2} J_{m-(\nu+1)/2}(x_\alpha) \\ -e^{-i(\nu-1)\theta/2} J_{m-(\nu-1)/2}(x_\alpha) \\ ic_\alpha e^{i(\nu-1)\theta/2} J_{m+(\nu-1)/2}(x_\alpha) \\ c_\alpha e^{i(\nu+1)\theta/2} J_{m+(\nu+1)/2}(x_\alpha) \end{pmatrix}, \quad (5)$$

where we use polar coordinates, the four-spinor convention $(\psi_\uparrow, \psi_\downarrow, \psi_\downarrow^\dagger, -\psi_\uparrow^\dagger)$ in spin and particle-hole space, and a normalization factor \mathcal{N}_α .

The superconducting boundary condition at $r = R$ leads to the conditions

$$\frac{J_{m-(\nu-1)/2}(x_\alpha) J_{m+(\nu+1)/2}(x_\alpha)}{J_{m-(\nu+1)/2}(x_\alpha) J_{m+(\nu-1)/2}(x_\alpha)} = 1, \quad (6)$$

$$c_\alpha = \frac{J_{m-(\nu+1)/2}(x_\alpha)}{J_{m+(\nu+1)/2}(x_\alpha)}.$$

Once the energies ϵ_α solving the first (implicit) equation in Eq. (6) have been determined, the coefficients c_α follow from the second equation. In addition, the spectral problem admits ν zero-energy solutions, where an even number of such states can hybridize to form topologically trivial Andreev bound states and one finds a single MBS for odd ν . In particular, for $\nu = 1$, the zero-energy state

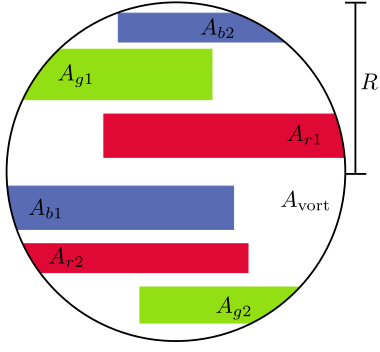


FIG. 1. TI vortex setup with six finger gates placed within the vortex core region of radius R . The gates cover areas of different sizes, A_{cj} , and are arranged in three pairs indicated by the colors $c \in \{r, b, g\}$. Gates forming a pair are referenced by $j \in \{1, 2\}$.

(with $m = n = 0$) is given by

$$f_{0,0}^{(\nu=1)}(\mathbf{r}) = \frac{1}{\sqrt{2}} \begin{pmatrix} 0 \\ -1 \\ i \\ 0 \end{pmatrix}, \quad (7)$$

while for $\nu = 2$, we find zero-energy states with angular momentum $m = \pm 1/2$,

$$f_{0,-1/2}^{(\nu=2)}(\mathbf{r}) = \sqrt{\frac{2}{3\pi}} \begin{pmatrix} 0 \\ e^{-i\theta}r/R \\ -i \\ 0 \end{pmatrix}, \quad (8)$$

$$f_{0,1/2}^{(\nu=2)}(\mathbf{r}) = \sqrt{\frac{2}{3\pi}} \begin{pmatrix} 0 \\ i \\ e^{i\theta}r/R \\ 0 \end{pmatrix},$$

which combine to form an Andreev bound state.

Next, we discuss the matrix elements of the disorder potential in the basis diagonalizing H_{BdG} ,

$$V_{\alpha\beta} = \int d\mathbf{r} f_{\alpha}^{\dagger}(\mathbf{r}) V(\mathbf{r}) \tau_z f_{\beta}(\mathbf{r}). \quad (9)$$

In order to avoid the explicit evaluation of the slowly converging and computationally intensive spatial integrals in Eq. (9), we use the fact that, since $V(\mathbf{r})$ is Gaussian distributed, the matrix elements $V_{\alpha\beta}$ have only non-trivial second moments. However, these matrix elements are correlated and therefore the full covariance matrices $\langle V_{\alpha\beta} V_{\gamma\delta}^* \rangle$ and $\langle V_{\alpha\beta} V_{\gamma\delta} \rangle$ are needed, where angular momentum conservation implies

$$\begin{aligned} \langle V_{\alpha\beta} V_{\gamma\delta}^* \rangle &\propto \delta_{m_{\alpha}-m_{\beta}, m_{\gamma}-m_{\delta}}, \\ \langle V_{\alpha\beta} V_{\gamma\delta} \rangle &\propto \delta_{m_{\alpha}-m_{\beta}, -(m_{\gamma}-m_{\delta})}. \end{aligned} \quad (10)$$

We note that matrix elements involving zero-energy states also satisfy Eq. (10). With $\Delta m_{\alpha\beta} = m_{\alpha} - m_{\beta}$, we next observe that $\langle V_{\alpha\beta} V_{\gamma\delta}^* \rangle \neq 0$ only if $\Delta m_{\alpha\beta} = \Delta m_{\gamma\delta}$. Similarly, $\langle V_{\alpha\beta} V_{\gamma\delta} \rangle \neq 0$ requires $\Delta m_{\alpha\beta} = -\Delta m_{\gamma\delta}$. Clearly, both covariances can be finite only for a disjoint set of disorder elements unless $\Delta m_{\alpha\beta} = \Delta m_{\gamma\delta} = 0$. It is then convenient to define

$$W_{\alpha\beta} = \begin{cases} V_{\alpha\beta}, & \Delta m_{\alpha\beta} > 0, \\ V_{\alpha\beta}^*, & \Delta m_{\alpha\beta} < 0, \\ V_{\alpha\beta} + i(V_{\alpha\beta}')^*, & \Delta m_{\alpha\beta} = 0, \end{cases} \quad (11)$$

with statistically independent auxiliary variables $V_{\alpha\beta}'$ (not entering the Hamiltonian) which are distributed identically as $V_{\alpha\beta}$. The new variables $W_{\alpha\beta}$ fulfill $\langle W_{\alpha\beta} W_{\gamma\delta} \rangle = 0$, and therefore the problem has been reduced to a single Hermitian covariance matrix, $C_{\alpha\beta\gamma\delta} = \langle W_{\alpha\beta} W_{\gamma\delta}^* \rangle$. Using a singular value decomposition, $C = U\Sigma U^{\dagger} = LL^{\dagger}$ with $L = U\sqrt{\Sigma}$, we can then map a set of *independent* normal-distributed complex elements, $X_{\alpha\beta}$, onto correlated matrix elements, $W_{\alpha\beta} = (LX)_{\alpha\beta}$. By using the inverse mapping of Eq. (11), one obtains the matrix elements $V_{\alpha\beta}$ in a numerically efficient manner. We have verified that disorder matrices generated by this mapping obey the same distribution as the spatial integrals in Eq. (9).

We finally describe the simulated gate setup used for generating the data in Fig. M3, which is illustrated in Fig. 1 and contains six finger gates inside the vortex with area $A_{\text{vort}} = \pi R^2$. The gates are paired up into $f = 3$ pairs, where each gate covers the area A_{cj} , with $c \in \{r, b, g\}$ indicating the “color” of a pair and $j \in \{1, 2\}$ numbering both gates forming the pair. The latter are assumed to be oppositely charged by means of opposite gate voltage shifts, $\pm \delta V_c$. Discretizing the vortex area A_{vort} into a grid of infinitesimal area pieces δA , the perturbation strength due to a gate pair with voltage changes $\pm \delta V_c$ can be estimated by summing over this spatial grid, where the gate voltage is constant for each finger gate and zero elsewhere. We then arrive at

$$\langle \Psi | \delta V_c | \Psi \rangle \approx \frac{\delta V_c}{A_{\text{vort}}} (A_{c1} - A_{c2}) = r_c \delta V_c. \quad (12)$$

Equation (12) defines the area fraction, $r_g = r_c$, for this gate pair. Independently tuning gate voltages on different gate pairs allows one to sample many disorder realizations, where an uncorrelated new sample is reached by varying the respective gate voltage by $\delta V_c \approx \delta_{\epsilon}/r_c$.